

Pretty Good Measurement for Radiomics: A Quantum-Inspired Multi-Class Classifier for Lung Cancer Subtyping and Prostate Cancer Risk Stratification

Giuseppe Sergioli¹, Carlo Cuccu¹, Giovanni Pasini^{2,3}, Alessandro Stefano^{2,3},
Giorgio Russo^{2,3}, Andrés Camilo Granda Arango¹, Roberto Giuntini¹

¹Università degli Studi di Cagliari, Via Is Mirrionis 1, Cagliari, 09123, Italy

²Institute of Bioimaging and Complex Biological Systems - National Research Council (IBSBC - CNR), Cefalù, 90015, Italy

³National Laboratory of South, National Institute for Nuclear Physics(LNS-INFN), Catania, 95125, Italy

Abstract

We investigate a quantum-inspired approach to supervised multi-class classification based on the *Pretty Good Measurement* (PGM), viewed as an operator-valued decision rule derived from quantum state discrimination. The method associates each class with an encoded mixed state and performs classification through a single POVM construction, thus providing a genuinely multi-class strategy without reduction to pairwise or one-vs-rest schemes. In this perspective, classification is reformulated as the discrimination of a finite ensemble of class-dependent density operators, with performance governed by the geometry induced by the encoding map and by the overlap structure among classes.

To assess the practical scope of this framework, we apply the PGM-based classifier to two biomedical radiomics case studies: histopathological subtyping of non-small-cell lung carcinoma (NSCLC) and prostate cancer (PCa) risk stratification. The evaluation is conducted under protocols aligned with previously reported radiomics studies, enabling direct comparison with established classical baselines. The results show that the PGM-based classifier is consistently competitive and, in several settings, improves upon standard methods. In particular, the method performs especially well in the NSCLC binary and three-class tasks, while remaining competitive in the four-class case, where increased class overlap yields a more demanding discrimination geometry. In the PCa study, the PGM classifier remains close to the strongest ensemble baseline and exhibits clinically relevant sensitivity–specificity trade-offs across feature-selection scenarios.

These findings support the relevance of PGM-based quantum-inspired decision rules as a mathematically well-motivated and practically viable extension of quantum state discrimination techniques to genuinely multi-class learning problems, and provide further evidence of their applicability in high-dimensional biomedical settings.

1 Introduction

In recent years, quantum computing has progressively moved beyond a purely programmatic phase and has become an area of research and development in which theoretical results, device engineering, and experimentation advance jointly [1, 2]. Today, hardware platforms can execute non-trivial sequences of quantum operations, grounded in formally characterized universal gate structures [3], and produce experimental data that are useful both for testing foundational ideas and for assessing, in a controlled way, the performance and limitations of the available systems.

At the same time, it is widely acknowledged that the path toward fully reliable, large-scale quantum machines remains demanding. The effects of noise and the fragility of quantum states impose stringent constraints, and many of the most ambitious promises depend on further progress in stability, control, and the ability to reduce errors. Nonetheless, the overall trajectory is clear: quantum computing is taking shape as a mature field, in which long-term objectives and medium-term applications coexist, and in which a realistic assessment of what is possible today proceeds hand in hand with the definition of future prospects [4, 5].

Against this background, advances in quantum computing have made it natural to ask not only whether and when quantum devices will be able to offer an advantage over classical computation,

but also in which application domains such an advantage (or even simply a practical benefit) might emerge in a more plausible and measurable way [6, 5, 7]. In particular, the availability of increasingly controllable experimental platforms has encouraged a shift in perspective: from the mere demonstration of principles and theoretical prototypes to the search for contexts in which real information-processing procedures can be reconsidered in light of the quantum resources currently accessible, including alternative logical and algebraic frameworks inspired by quantum computational structures [8], while still taking into account the limitations that remain (noise, stability, scalability).

Among these contexts, machine learning has emerged as an almost inevitable candidate. On the one hand, machine learning originates and develops precisely in response to the need to extract structure and information from large volumes of data, in settings where computational cost and model complexity rapidly become dominant. On the other hand, quantum computing has been conceived, since its original motivations, as a paradigm capable of treating more efficiently certain classes of computationally demanding problems.

The convergence of these two trajectories has led to the emergence of quantum machine learning (QML) as an autonomous area: a research program that aims to reformulate certain learning procedures in a natively quantum language, leveraging specific physical resources of quantum computation. In particular, the possibility of expressing crucial subroutines in terms of unitary operators and controlled quantum dynamics sustains the expectation that, at least in principle and for certain classes of tasks, such reformulations may translate into concrete and relevant computational speed-ups with respect to classical implementations, especially when the latter rapidly become prohibitive in terms of complexity and resources.

However, the application of quantum computing to machine learning does not exhaust the ways in which quantum theory can be put to work in this context. Alongside the properly quantum line—in which learning procedures are reformulated to be executed on quantum devices—a second strand has developed, often referred to as quantum-inspired (or quantum-like) machine learning. In this case, the inspiration comes from concepts and tools of quantum information theory, but the algorithms remain formulated in classical language and are executable on conventional computers. It follows that the objective is not primarily the speed-up linked to quantum hardware, but rather the introduction of conceptual schemes and design criteria that can guide the construction of alternative and potentially more effective learning methods.

A particularly natural source of inspiration, already discussed in the literature, is quantum state discrimination. In quantum theory, discriminating states means rigorously formalizing the distinguishability among physical preparations and deriving optimal decision procedures under conditions of unavoidable uncertainty. In the quantum-inspired setting, this perspective suggests reinterpreting the classification problem as a “discrimination” task among class representatives, adopting decision criteria motivated by the notion of distinguishability. Along this line, the expected benefit does not concern so much a reduction in computational complexity, but rather the possibility of achieving good levels of accuracy through decision rules that inherit, in classical form, the discriminative intuition characteristic of the quantum framework.

From this perspective, interest in quantum-inspired machine learning does not remain confined to a conceptual proposal: some early lines of research have in fact shown how a binary classifier inspired by state discrimination can be transferred in a natural way to concrete problems [9, 10], where the quality of the decision (more than computational efficiency alone) is a central requirement. In the biomedical domain, this requirement is particularly stringent: data are often heterogeneous and noisy, and class separation may depend on weak signals or on patterns that are not immediately evident.

Against this background lie the first attempts to apply the quantum-inspired classifier to practical cases. On the one hand, the approach has been explored on clinical data in a pulmonary context, for instance for classification tasks related to survival stratification in patients with idiopathic pulmonary fibrosis, where discrimination among classes assumes a directly interpretive relevance. On the other hand, image analysis has been considered in laboratory procedures—for example in supporting the evaluation of clonogenic assays—where the crucial task is a binary discrimination (colony vs. background) that affects the final quantification [11].

The experiments discussed so far had an intrinsically binary setting, because they were based on a quantum-inspired classifier derived directly from the Helstrom measurement, which arises as the optimal (minimum-error) solution to the problem of discriminating between two states: in machine learning terms, this translates into a natural device for two-class classification. In the presence of more classes, such an approach therefore tends to require decomposition strategies (e.g., one-vs-one or one-vs-rest), with a consequent multiplication of comparisons and required resources.

More recently, however, a quantum-inspired classifier natively n -ary has been proposed, which addresses multi-class classification directly, without reducing it to a collection of binary problems [12, 13]. The guiding idea remains that of quantum state discrimination, but the extension to

the general case is obtained by adopting the *Pretty Good Measurement* (PGM), i.e., a systematic procedure to construct a measurement (POVM) capable of discriminating an arbitrary set of states with a good probability of success. This shift is conceptually relevant: on the one hand, it makes the treatment of datasets with multiple labels “natural”; on the other hand, precisely because the method is formulated in the language of quantum measurement theory, it also suggests possible implementations on quantum hardware (at least in principle), in addition to immediate execution on conventional computers in a quantum-inspired form.

In an applicative perspective, this opens in a particularly direct way to the possibility of addressing multi-class biomedical problems, where classification rarely reduces to a simple “yes/no” and where, instead, it is often crucial to distinguish among multiple conditions, phenotypes, or levels of severity within the same clinical or experimental framework.

In this work, we consider two biomedical scenarios already well characterized in the literature and based on imaging and radiomics data. The first concerns the phenotyping of histopathological subtypes of Non-Small-Cell Lung Carcinoma (NSCLC) from multicenter Computerized Tomography (CT) images [14], where the clinical-informative goal is to distinguish among multiple subtypes (e.g., Adenocarcinoma, Squamous Cell Carcinoma, Large Cell Carcinoma, and a “Not Otherwise Specified” class), in a context in which acquisition variability and pipeline choices substantially affect the difficulty of the task. The second scenario concerns the stratification of risk in prostate carcinoma from images of Prostate-Specific Membrane Antigen (PSMA) and positron emission Tomography (PET/CT)[15], in which the basic setting is aimed at separating grouping of patients according to clinically significant risk classes, with the aim of supporting diagnostic and therapeutic decisions in a non-invasive way.

The objective of the article, in continuity with what has been discussed above about the transition from binary schemes to a natively n -ary classifier inspired by the PGM, is to show how this approach can be applied in a multi-class mode to the datasets and contexts considered in these two works, directly treating the multi-class problem (without one-vs-one or one-vs-rest strategies) and discussing in a transparent way the methodological implications and the empirical behavior on the biomedical data under examination.

The paper is organized as follows. First, to make the presentation self-contained, we provide a concise but technically explicit account of the PGM-based discrimination protocol as it is used for supervised classification. We then summarize, at a qualitative level but with the essential experimental details, the two reference applications that serve as our clinical and methodological benchmarks, namely prostate cancer and lung carcinoma. The second part of the paper is devoted to our main contribution: we report the results of applying the PGM-based quantum-inspired classifier to these two medical-imaging radiomics datasets, under evaluation protocols chosen to enable a meaningful comparison with baselines previously obtained with classical methods. The paper closes with some final remarks.

2 The Pretty Good Measurement (PGM) classifier

In this section we summarize the multi-class quantum-inspired classifier based on the PGM, presenting the construction in a self-contained form while keeping the notation close to standard supervised learning.

Let $L = \{1, \dots, \ell\}$ be the set of class labels, and let a training dataset be a finite set

$$S_{\text{tr}} = \{(x_1, \lambda_1), \dots, (x_m, \lambda_m)\}, \quad \lambda_j \in L, \quad (1)$$

where each object is represented by a feature vector $x_j \in \mathbb{C}^d$ (the real-valued case is included as a special instance).

We represent multi-class prediction by assigning a score to each class. Concretely, we specify a scoring function

$$f : \mathbb{C}^d \rightarrow [0, 1]^\ell, \quad f(x) = (f_1(x), \dots, f_\ell(x)),$$

and define the associated classifier by selecting the label with the highest score:

$$Cl_f(x) := \min \left\{ i \in L : f_i(x) = \max_{1 \leq k \leq \ell} f_k(x) \right\},$$

where, in case of ties (multiple maximizers), we choose the smallest index. As it will be shown, in the PGM classifier the scores are produced by a measurement rule and therefore admit a direct probabilistic interpretation.

The first quantum-inspired step consists in fixing an encoding (feature map) that associates to each input vector x a density operator ρ_x on a finite-dimensional Hilbert space $H \simeq \mathbb{C}^n$:

$$x \longmapsto \rho_x \in \mathcal{D}(H). \quad (2)$$

In previous works [9, 10] different kinds of encodings have been introduced (*amplitude* and *stereographic* encodings).

The encoding turns the classical training set into its encoded counterpart

$$\tilde{S}_{\text{tr}} = \{(\rho_{x_j}, \lambda_j)\}_{j=1}^m.$$

For each class $i \in L$, let $S_{\text{tr}}^i := \{x_j : \lambda_j = i\}$ and consider the corresponding family of encoded states $\tilde{S}_{\text{tr}}^i = \{\rho_{x_j} : x_j \in S_{\text{tr}}^i\}$.

Now we associate to each class i a single density operator that plays the role of a class representative.

This representative is taken to be the *quantum centroid*, i.e., the uniform average of the encoded training states in that class,

$$\rho^{(i)} := \frac{1}{|\tilde{S}_{\text{tr}}^i|} \sum_{x_j \in S_{\text{tr}}^i} \rho_{x_j}, \quad i \in L. \quad (3)$$

Even when the encoding produces pure states, the centroid $\rho^{(i)}$ is generally mixed, and its geometry need not coincide with that of classical centroids in feature space; this is one of the mechanisms by which the induced decision rule can depart from standard nearest-mean classifiers.

To turn these class representatives into a multi-class prediction rule, one uses a POVM-induced scoring function. A POVM with outcomes in L is a family of positive semidefinite operators $\{M_i\}_{i=1}^\ell$ on H such that $\sum_{i=1}^\ell M_i = I$. Given a POVM and an encoded input ρ_x , Born's rule produces scores

$$f_i(x) := \text{tr}(M_i \rho_x), \quad i \in L, \quad (4)$$

which satisfy $f_i(x) \in [0, 1]$ and $\sum_{i=1}^\ell f_i(x) = 1$.

The PGM specifies a canonical way to construct such a POVM from an ensemble of hypotheses. Consider the ensemble of class representatives with priors

$$\mathcal{R} = \{(p_1, \rho^{(1)}), \dots, (p_\ell, \rho^{(\ell)})\}, \quad p_i > 0, \quad \sum_{i=1}^\ell p_i = 1, \quad (5)$$

and define the average (mixture) state

$$\sigma := \sum_{i=1}^\ell p_i \rho^{(i)}. \quad (6)$$

The PGM elements are first defined on the support of σ by

$$E_i := \sigma^{-1/2} p_i \rho^{(i)} \sigma^{-1/2}, \quad i \in L, \quad (7)$$

where σ^{-1} denotes the Moore–Penrose pseudoinverse and $\sigma^{-1/2}$ its positive square root. In general $\sum_{i=1}^\ell E_i = P_{\text{im}(\sigma)}$, the projection onto the image of σ , and one obtains a proper POVM by completing on the kernel:

$$F_i := E_i + \frac{1}{\ell} P_{\text{ker}(\sigma)}, \quad i \in L. \quad (8)$$

Then $\sum_{i=1}^\ell F_i = I$, and the family $F = \{F_i\}_{i=1}^\ell$ defines a valid measurement. The corresponding scoring function and classifier are obtained by setting

$$f_i(x) := \text{tr}(F_i \rho_x), \quad \text{Cl}_{\text{PGM}}(x) := \min \left\{ i \in L : \text{tr}(F_i \rho_x) = \max_{1 \leq k \leq \ell} \text{tr}(F_k \rho_x) \right\}. \quad (9)$$

In the absence of externally imposed class priors, one may adopt uniform priors $p_i = 1/\ell$, so that the measurement is determined entirely by the geometry of the class centroids through σ . A key methodological point is that this construction is *intrinsically multi-class*: the decision rule arises from a single ℓ -outcome POVM and does not require one-vs-rest or one-vs-one decompositions.

An optional extension increases expressive power by lifting the representation via tensor copies. For $n \in \mathbb{N}_+$ one encodes an input as $\rho_x^{(n)} := \rho_x^{\otimes n}$ and defines class representatives as

$$\rho^{(i)} := \frac{1}{|S_{\text{tr}}^i|} \sum_{x_j \in S_{\text{tr}}^i} \rho_{x_j}^{\otimes n}, \quad (10)$$

noting that, in general, $\rho^{(i)} \neq (\rho^{(i)})^{\otimes n}$. The PGM construction is then repeated on the ensemble $\{(p_i, \rho^{(i)})\}_{i=1}^\ell$, yielding POVM elements $\{F_i^{(n)}\}_{i=1}^\ell$ and scores $f_i^{(n)}(x) = \text{tr}(F_i^{(n)} \rho_x^{\otimes n})$. Empirically,

increasing n may improve performance at the cost of higher computational load, since training requires forming σ and computing $\sigma^{-1/2}$ in the enlarged operator space. Once the measurement is fixed, inference reduces to evaluating the traces $\text{tr}(F_i \rho_x)$ (or their n -copy counterparts) and applying the argmax decision rule.

To further improve the classifier’s accuracy, in [9] we showed that two additional choices can be tuned already at the preprocessing stage. The first concerns the *encoding*, namely the map that associates each real feature vector x with a quantum state ρ_x . There are many admissible ways to construct such an encoding $x \mapsto \rho_x$ (e.g., via a direct real-vector representation or via a density-operator representation), and the most effective choice can be dataset-dependent. The second concerns the introduction of a multiplicative *rescaling factor* $\alpha > 0$, applied to all feature vectors before encoding (i.e., $x \mapsto \alpha x$). Empirically, this global rescaling can yield an additional gain in accuracy, which is consistent with the fact that the classification procedure takes place in the geometric state space of quantum states, where distances and overlaps depend on the chosen scale of the embedded data. Accordingly, an application of the PGM classifier can include a grid-search over the main hyperparameters discussed above, namely the encoding scheme, the number of copies, and the rescaling factor.

3 Clinical Imaging Baselines: Radiomics Pipelines and Reported Performance on Lung Carcinoma and Prostate Cancer Datasets

Radiomics is an emerging field that transforms medical images into high-dimensional, mineable data by extracting a large number of quantitative features [16] that capture properties of a lesion or tissue region. Instead of relying solely on visual interpretation, radiomics transforms images into measurable data, enabling more objective and reproducible analyses. These features typically fall into three main categories: Shape features, which describe the 3-D geometry of a lesion (e.g., volume, sphericity), first-order features, which summarize the distribution of voxel intensities (e.g., mean, variance, entropy), and texture features, which quantify spatial patterns and heterogeneity within the image by analyzing relationships between neighboring voxels.

By converting images into hundreds or thousands of these numerical variables, radiomics allows subtle imaging patterns, often imperceptible to the human eye, to be linked with biological characteristics, clinical outcomes, or treatment response. In CT imaging, radiomics enables a detailed characterization of tissue heterogeneity, supporting improved diagnosis, tumor phenotyping, and treatment response prediction. When integrated with PET/CT, radiomics leverages both anatomical information from CT and metabolic activity from PET, allowing a more comprehensive assessment of tumor biology [17]. An example for the two imaging modalities (i.e., CT and PET/CT) and two considered case studies (NSCLC and Prostate, that will be detailed in Section 4) is shown in Figure 1.

A substantial body of recent work has demonstrated that both quantum machine learning and quantum-inspired methodologies can be meaningfully stress-tested on real-world biomedical datasets, with medical imaging emerging as a particularly stringent domain because it combines high dimensionality, acquisition-driven variability, and clinically constrained sample sizes [18, 19, 20, 21, 22, 11].

In this context, the two medical studies that motivate the present work provide complementary baselines. The first one investigates the feasibility and limitations of applying radiomics to multicenter CT datasets for the phenotyping of NSCLC subtypes [14]. NSCLC represents the predominant form of lung malignancy, accounting for roughly 85% of all diagnosed cases, in contrast to the less common small-cell lung cancer (SCLC) [23]. According to the World Health Organization classification, NSCLC encompasses three principal histological subtypes: Adenocarcinoma (ADC, approximately 40% of cases), Squamous Cell Carcinoma (SCC, about 25–30%), and large-cell carcinoma (LCC, around 5–10%). Diagnostic uncertainties, however, have led to the introduction of an additional category—termed “Not Otherwise Specified” (NOS)—used for tumors that cannot be confidently assigned to any of the major subgroups based on available clinical or pathological criteria.

Using two public databases, the authors extracted IBSI-compliant (Image Biomarker Standardisation Initiative) [24] radiomics features from manually and segmented lesions. The IBSI is an international effort aimed at establishing standardized definitions, nomenclature, and computational procedures for radiomics feature extraction. Its goal is to ensure that radiomics biomarkers are computed consistently and reproducibly across different software tools, imaging modalities, and research centers. By providing formal mathematical definitions, benchmark datasets, and reference values, IBSI helps improve the transparency, comparability, and clinical reliability of radiomics

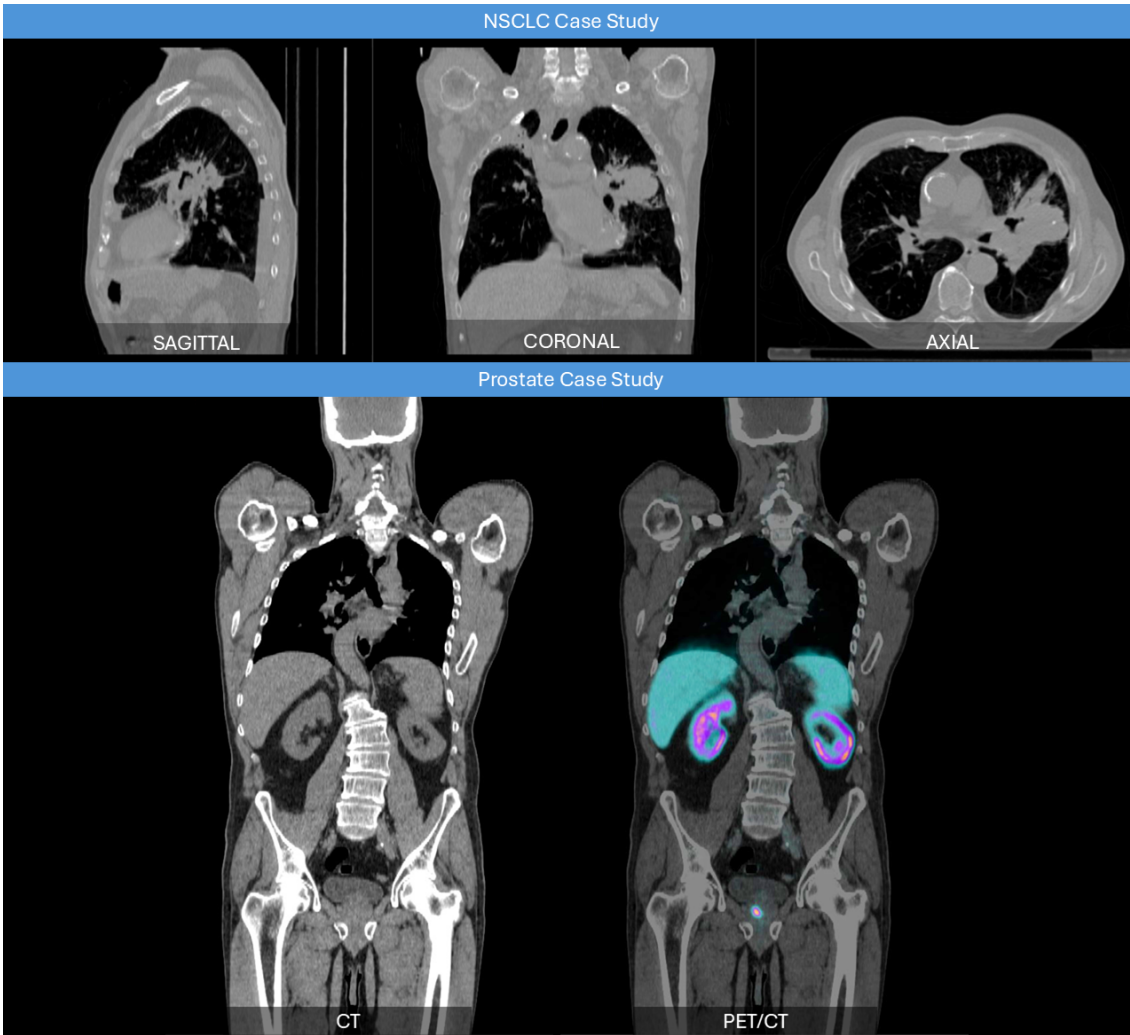


Figure 1: In the first row (NSCLC Case Study) there is an example of CT at the three anatomical planes: sagittal (left), coronal (middle), axial (right). In the second row, there is an example of CT (on the left) and PET/CT (on the right) for the Prostate Case Study. PET/CT highlights high metabolic areas, in this case in the liver, kidneys, spleen and a focal spot in the prostate.

studies.

A central focus of the work presented in [14] is the quantitative characterization of batch effects stemming from heterogeneous CT acquisition protocols, differences in scanner vendors, and variability in segmentation workflows. Through statistical analyses, the authors show that multicenter radiomics datasets tend to cluster primarily according to the acquisition site rather than the underlying tumor phenotype, even after applying standard preprocessing steps such as isotropic voxel resampling. Consequently, the ComBat harmonization technique [25] is employed to strike a balance between mitigating batch effects and preserving biologically meaningful discriminative information. Downstream learning is carried out using a repeated outer-loop approach based on multiple stratified 80/20 train–test splits. Within each outer loop, feature selection is performed exclusively on the training folds through a two-step procedure: an initial Kruskal–Wallis screening, followed by the Least Absolute Shrinkage and Selection Operator (LASSO) [26]. LASSO is among the most widely adopted radiomics feature-reduction methods, as it enables the extraction of a compact set of stable and informative predictors while effectively limiting overfitting—a critical concern given the high feature-to-sample ratio that characterizes multicenter datasets. Model selection and hyperparameter optimization are handled by repeated 5-fold cross-validated Bayesian optimization. Six different classification models are compared using the harmonized datasets: Discriminant Analysis (DC), K-Nearest Neighbors (KNN), Support Vector Machines (SVM), Naïve Bayes (NB), Decision Trees (TREE), and Ensemble methods. The reported outcomes highlight the intrinsic difficulty of multi-class radiomics phenotyping at scale. Accuracy is lowest when the models are tasked with the most complex scenarios: the four-class task (distinguishing between Squamous Cell Carcinoma, Adenocarcinoma, Large Cell Carcinoma, and “Not Otherwise Specified”) and the three-class task (excluding the “Not Otherwise Specified” group). In these instances, the Ensemble model is the most effective, achieving accuracies of 56.2% and 52.9%, respectively. The

most significant performance gains occurred in the simplest scenario: a binary classification between the two most common subtypes, Squamous Cell Carcinoma and Adenocarcinoma. In this case, the performance of all classifiers is closely aligned, ranging from a minimum accuracy of 56.25% (DC) and a maximum accuracy of 58.57% (NB). In terms of the Area Under the Curve (AUC), the Ensemble model consistently yields the strongest results across every classification task. It achieves a notable AUC of 95.7% for the “Not Otherwise Specified” class. For the other subtypes, AUC values ranged from 61.48% to 79.9% for Adenocarcinoma, 65.8% to 69.1% for Squamous Cell Carcinoma, and 70.6% to 73.0% for Large Cell Carcinoma.

The second study focuses on PET/CT-based radiomics in nuclear medicine for prostate cancer (PCa) risk stratification [15]. As the second most frequent cancer in men globally, PCa management relies heavily on accurate staging to prevent overtreatment. While Prostate-Specific Antigen (PSA) levels are standard for screening, PSA is organ-specific rather than tumor-specific; its elevation in benign conditions often leads to unnecessary biopsies, which carry clinical risks such as hematuria, infection, and sepsis [27, 28]. Definitive risk stratification has traditionally relied on the Gleason score (GS), a histological grading system (ranging from 1 to 5) assigned to the two most prevalent patterns in a biopsy sample. Under this system, patients are categorized into:

1. Low-Risk: $GS \leq 6$, indicating low metastatic potential.
2. Intermediate-Risk: $GS = 7$
3. High-Risk: $8 \leq GS \leq 10$, indicating highly aggressive tumors.

However, GS is limited by biopsy sampling bias, as it may fail to characterize the whole tumor volume or its inherent heterogeneity. To overcome these limitations, imaging targeting the PSMA, a transmembrane glycoprotein significantly upregulated in malignant PCa cells, has been introduced. This imaging modality utilizes radiotracers, biologically active molecules labeled with a positron-emitting radionuclide. Once injected, they bind to specific molecular targets to allow non-invasive visualization and quantification of biochemical processes. While ^{68}Ga tracers are common, ^{18}F -PSMA-1007 has emerged as a superior radiopharmaceutical due to its longer half-life and optimized energy profiles, facilitating more accurate localization and staging [29]. The PCa study [15] addresses these clinical needs by focusing on binary risk stratification using ^{18}F -PSMA-1007 PET/CT data. In a retrospective cohort where tumor regions were manually delineated, radiomics features are extracted following Standardized Uptake Value (SUV) normalization, as reported in [30]. The SUV is the most common semi-quantitative parameter used to estimate biodistribution in PET images. The SUV normalizes the voxel activity considering acquisition time, administered activity, and patient weight. In this way, PET images took into account factors that would otherwise be ignored during radiomics analysis. The key contribution of [15] lies in the explicit operationalization of robustness with respect to dataset variability. A preliminary pipeline—iterated 30 times and comprising an 80/20 stratified split, LASSO-based feature selection, and five-fold cross-validation for Bayesian hyperparameter optimization—serves to identify stable features and to define a pool of candidate base learners. Subsequently, an ensemble model is constructed and evaluated across the same repeated splits. Trained on a feature set that combines highly frequent “robust” predictors with a decorrelated subset of moderately frequent “fine-tuning” features, the ensemble achieves the strongest average test performance: an accuracy of 79.52% and an AUC of 85.75%.

Taken together, these two baselines illustrate the potential of state-of-the-art radiomics: they show that competitive performance is attainable through rigorous validation, stability-aware feature selection, and explicit treatment of acquisition-driven heterogeneity. At the same time, they expose the bottlenecks that motivate the present work—most notably, the fragility of multi-class structures in high-dimensional representation spaces. These characteristics render the datasets ideal benchmark testbeds for evaluating whether quantum-inspired multi-class decision rules can provide a more principled inductive bias under realistic clinical constraints.

4 Materials and Methods

In this section we present the results of a direct comparison between the experiments described in the previous section and the PGM-based approach. The PGM classifier is evaluated on the same datasets introduced above, using a matched experimental setting, and its performance is reported side by side with the baseline results.

4.1 Dataset Description and Image Processing

This section describes the datasets and the processing procedures adopted to benchmark the proposed quantum-inspired classifier. The analysis focuses on the two clinical scenarios introduced earlier:

phenotyping of NSCLC and risk stratification in PCa. Starting from CT images in the first scenario and PET/CT images in the second, the overarching aim was to quantitatively characterize the target lesions through a standardized radiomics workflow built upon the *matRadiomics* framework [31]. *matRadiomics* is a comprehensive, IBSI-compliant radiomics platform designed to support the entire analytical pipeline — from image visualization, to the segmentation process, to image pre-processing, to feature extraction, to data harmonization and predictive modeling. Built on the PyRadiomics [32], it enables the standardized computation of 1,781 high-dimensional features, including shape descriptors, first-order statistics, and a broad set of texture features derived from the Gray Level Co-occurrence Matrix, Gray Level Run Length Matrix, Gray Level Size Zone Matrix, Neighboring Gray Tone Difference Matrix, and Gray Level Dependence Matrix. For both CT and PET modalities, features were then extracted from three complementary image representations:

1. Original biomedical images,
2. Laplacian of Gaussian (LoG) filtered images, and
3. Multilevel wavelet-decomposed images.

matRadiomics ensures high reproducibility, transparent control of preprocessing parameters, and robust handling of multicenter data through built-in batch-effect detection and correction tools such as ComBat harmonization, an essential component when working with heterogeneous acquisition protocols [17]. The specific configurations for the two studies are detailed in the following subsections.

4.1.1 Non-Small-Cell Lung Carcinoma (NSCLC) Dataset

The lung cancer cohort was established by merging two public repositories: the NSCLC-Radiomics and NSCLC-Radiogenomics datasets, resulting in 466 patients categorized into four histopathological subtypes: Squamous Cell Carcinoma (SCC, $n = 152$), Adenocarcinoma (ADC, $n = 150$), Large Cell Carcinoma (LCC, $n = 106$), and Not Otherwise Specified (NOS, $n = 58$). To evaluate the proposed classifier across different diagnostic complexities, the original cohort was partitioned into three distinct datasets with varying labeling schemes:

- A **4-classes dataset** (4-c) comprising all histopathological subtypes (SCC, ADC, LCC, and NOS; $n = 466$).
- A **3-classes dataset** (3-c) excluding the NOS subtype ($n = 408$).
- A **2-classes dataset** (2-c) focusing on the most prevalent subtypes, Squamous Cell Carcinoma and Adenocarcinoma ($n = 302$).

To mitigate batch effects inherent in multicenter CT data acquired from different manufacturers (Siemens, CMS, GE, Philips), images were resampled to an isotropic voxel size of $1 \times 1 \times 1 \text{ mm}^3$ using linear interpolation. The volumes of interest (VOIs) to be examined were provided together with the CT images. Feature harmonization was subsequently performed via the ComBat tool to standardize the mean and variance across the different acquisition centers.

4.1.2 Prostate Cancer (PCa) Dataset

The dataset included patients who underwent PSMA (Prostate-Specific Membrane Antigen) -1007 PET/CT imaging for PCa staging. All subjects were retrospectively selected according to predefined inclusion criteria, namely: histologically confirmed PCa, availability of Gleason grade, and a positive PET scan. Patients previously treated with surgery, radiotherapy, chemotherapy, endocrine therapy, or with a history of other malignancies were excluded. The final cohort comprised 143 patients, stratified according to the Gleason grading system (72 with high-risk and 71 with low-risk). PET/CT acquisitions were acquired approximately 120 minutes after tracer injection. Manual slice-by-slice segmentation was performed by experienced clinicians to define the VOIs.

4.2 Experimental Protocol

To ensure the comparability of our results with existing benchmarks, we adopted the data partitioning and pre-processing frameworks established in previous studies by Pasini *et al.* [14, 15].

For the NSCLC study, our experimentation utilized the identical feature-selected and harmonized data splits from the original study (comprising 10 repetitions). This framework was applied to three distinct classification tasks with varying histopathological granularity—namely, **4-class** (SCC, ADC, LCC, NOS), **3-class** (SCC, ADC, LCC), and **binary** (SCC vs. ADC) datasets—as detailed in Subsection 4.1.1. For each classification task, we implemented an optimization protocol

consisting of 10 repetitions of the grid search with stratified 5-fold cross-validation on the training set to determine the optimal hyperparameters (optimizing for AUC), using the parameter space detailed in Table 1. The optimized model was then evaluated on the independent test set. To ensure statistical stability, performance metrics were first averaged across the ten iterations of the 5-fold cross-validation within each split, and then the final results were obtained by averaging these values across all ten splits.

For the prostate cancer dataset, the experimental protocol was designed to ensure full consistency with the benchmarking ensemble model by adopting the exact 30 stratified train/test splits (80/20 ratio) established in the reference study by Pasini *et al.* [15]. This approach enabled the use of pre-calculated feature frequency data from 30 iterations of the LASSO selection process, replicating the 13 feature subsets employed in the original experimentation. These subsets include eleven frequency-based groups (generated using thresholds from $\geq 90\%$ down to 0% , including an additional 5% threshold) and two specialized subsets: the *finetuning* subset (features with selection frequency between 30% and 70% , uncorrelated with the most robust features) and the *features7030r* subset (a union of *finetuning* and *features70*).

Hyperparameter optimization was performed using a grid search approach with stratified 5-fold cross-validation on the training sets, with the parameter space defined in Table 1, using the Area Under the Curve (AUC) as the objective metric. The most robust configuration was selected based on two criteria: (1) the frequency of occurrence across the 30 independent runs, and (2) in cases of ties, the mean test-set AUC achieved by each candidate configuration. This two-step selection process ensures both stability across diverse data partitions and optimal predictive performance, mitigating bias toward any specific data split. According to this criterion, the most frequently selected configuration employed amplitude-based encoding, no tensor copies of the feature vectors, and a rescaling factor of 0.5.

The classification performance on the test set for both datasets was evaluated using a comprehensive set of metrics. For the Lung Carcinoma study, we considered Accuracy and AUC per-class, while for the PCa study, the evaluation framework included Accuracy, AUC, Precision, Recall (Sensitivity), F1-score, and Specificity, ensuring a rigorous assessment of the model’s ability to distinguish between high-risk and low-risk patients.

Table 1: Hyperparameter space employed for grid search in both classification tasks.

Encoding	Rescaling	Number of Copies
{stereo, amplit}	{0.5, 1, 2, 4, 8, 16}	{1, 5, 10, 15, 20, 25, 30, 35, 40, 45, 50, 55, 60}

5 Results

In this section we report the outcomes of the experiments conducted on the two benchmark datasets (NSCLC and PCa). For each dataset we present the evaluation metrics that enable a direct, quantitative comparison between our PGM classifier and the results reported in [14, 15].

Overall, the presented results demonstrate that our PGM approach attains competitive (and in several cases superior) performance relative to the state-of-the-art methods evaluated in the literature.

Due to privacy constraints, the datasets used and the algorithms developed during the experiments are available from the corresponding author upon reasonable request.

5.1 NSCLC Dataset

For the NSCLC dataset we provide three Figures (2, 3, and 4), one for each class configuration (2, 3, and 4 classes). Each figure reports the mean AUC computed over all data splits together with macro-averaged accuracy score for the PGM classifier and the classical machine learning models exploited by Pasini *et al.* [14]. For each labeling we also present a win-loss heatmap 5 that juxtaposes the conventional classifiers with the PGM classifier. The heatmap is generated by averaging the per-class AUC scores of each model across cross-validation folds, thereby illustrating the overall performance trend. Because only aggregate values are available for the baseline classifiers, statistical significance could not be evaluated.

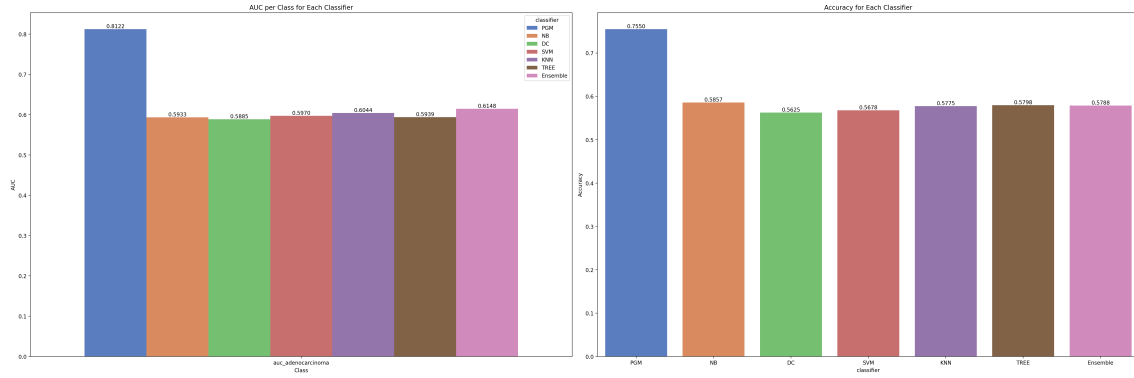


Figure 2: Comparative evaluation of the proposed PGM classifier against conventional baseline models on the NSCLC two-class dataset. (a) Mean test area under the ROC curve (AUC) reported for each class. (b) Macro-averaged accuracy across the two classes.

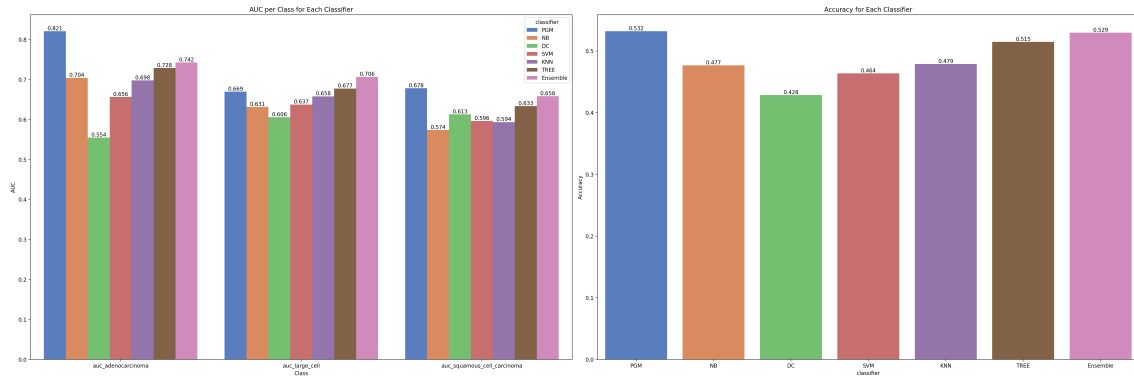


Figure 3: Comparative evaluation of the proposed PGM classifier against conventional baseline models on the NSCLC three-class dataset. (a) Mean test area under the ROC curve (AUC) reported for each class. (b) Macro-averaged accuracy across the three classes.

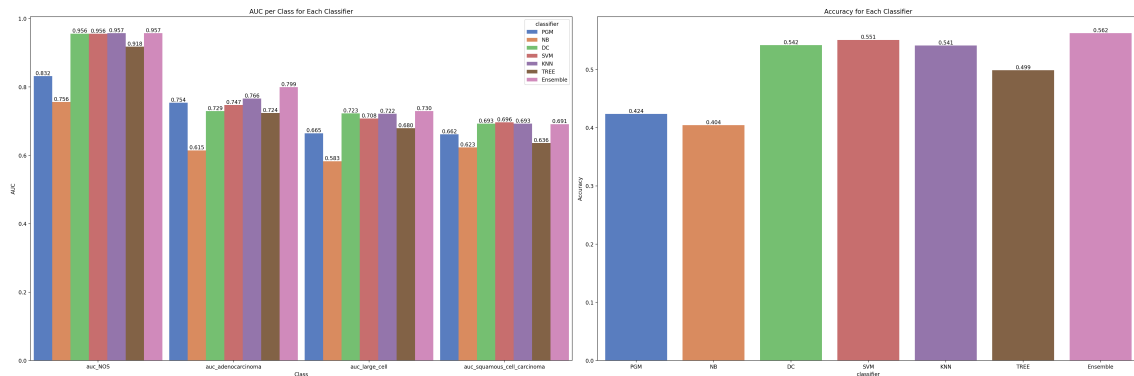


Figure 4: Comparative evaluation of the proposed PGM classifier against conventional baseline models on the NSCLC four-class dataset. (a) Mean test area under the ROC curve (AUC) reported for each class. (b) Macro-averaged accuracy across the four classes.

5.2 PCa Dataset

For the PCa dataset, Figure 6a shows the mean performance of the PGM classifier across the different feature-set variations. This plot allows a straightforward comparison with the quantum-inspired classifier and with the ensemble model results presented in Figure 6 of Pasini et al. [15]. Complementarily, Figure 6b presents a radar chart summarizing the six evaluation metrics across feature-selection scenarios. This representation provides an integrated view of the multidimensional performance profile of the PGM classifier and facilitates an immediate qualitative comparison of the balance among the considered metrics. To highlight the relative behaviour of the two approaches across the 13 predefined feature subsets, we compute the element-wise difference of the six performance metrics (Accuracy, AUC, Sensitivity, Specificity, Precision, F-score) between the PGM and the Ensemble models. The resulting matrix is visualised in Figure 7. The heat-map employs a diverging blue–red colour map centred at zero: blue cells indicate a positive difference (PGM

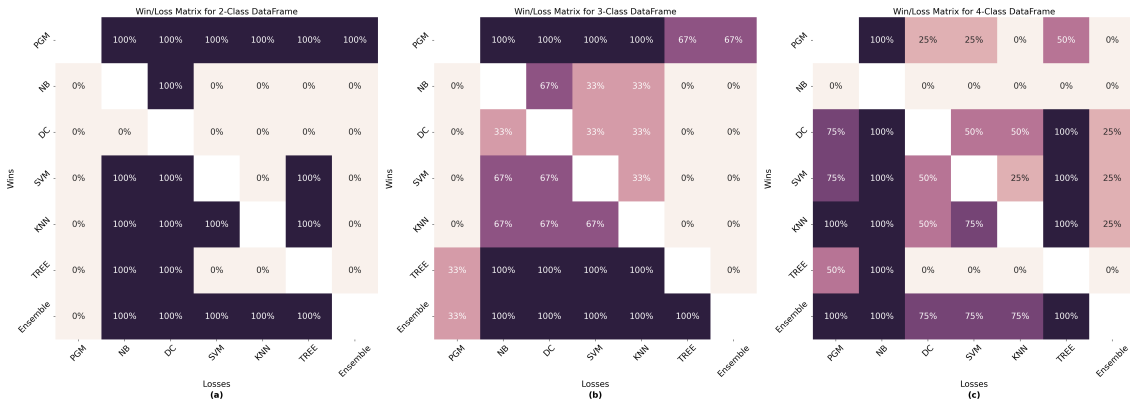
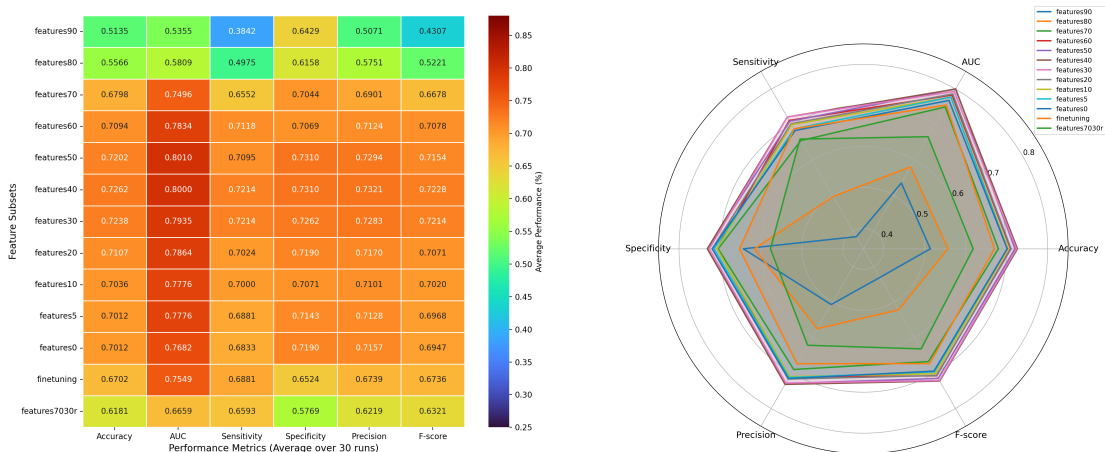


Figure 5: Win-loss heatmap comparing classifiers for each labeling scenario. The three labeling scenarios are: (a) 2-class labeling – only two disease categories are considered; (b) 3-class labeling – three distinct categories are distinguished; (c) 4-class labeling – all four histopathological subtypes are used. For each pair of classifiers, each cell reports the proportion of classes for which the row classifier attains a higher AUC than the column classifier. Values therefore range from 0% to 100% and indicate the fraction of class-wise pairwise wins. Warmer colors denote a larger proportion of class-level dominance.



(a) Mean performance of the PGM classifier across feature-set variations, averaged over 30 iterations using the same test-set subdivision of the original study.

(b) Radar chart summarizing the six evaluation metrics across feature-selection scenarios.

Figure 6: Performance analysis of the PGM classifier on the PCa dataset under different feature-selection scenarios.

outperforms the Ensemble), while red cells denote a negative difference (Ensemble outperforms PGM). The intensity of the colour is proportional to the magnitude of the difference, allowing a rapid visual assessment of the scenarios in which the quantum-inspired classifier provides a tangible advantage over the traditional ensemble method.

5.3 Discussion

The results reveal two distinct patterns across the considered datasets.

For the NSCLC dataset, the comparison is particularly informative. In the 2-class setting, the PGM classifier consistently improves upon all the classifiers considered in the previous study, showing gains both in terms of accuracy and in terms of ROC-based performance. The same trend is confirmed in the 3-class setting as well, although the advantage is somewhat less pronounced than in the binary case. In contrast, the picture changes in the 4-class setting: while PGM remains competitive, its superiority is no longer observed and it does not emerge as the best-performing classifier among those tested. We may interpret the decline in performance as the number of classes increases as a natural effect of the greater geometric complexity of the problem. In particular, when moving from 2 to 3–4 classes, it becomes more likely that some classes lie closer to one another — and thus overlap more — in the state space induced by the encoding; consequently, the distributions associated with different classes tend to be less clearly separated, and the discrimination



Figure 7: Heat-map of metric differences (PGM – Ensemble) across feature-selection scenarios. Each row corresponds to a feature-set, and each column represents one of the six evaluation metrics *Accuracy*, *AUC*, *Sensitivity*, *Specificity*, *Precision*, and *F-score*. Cells are coloured on a diverging blue–red scale centred at zero: A blue hue indicates that the PGM classifier outperforms the ensemble for that metric (positive difference), whereas a red hue denotes inferior performance (negative difference). The colour intensity is proportional to the magnitude of the difference, allowing a rapid visual assessment of where the quantum-inspired PGM model provides gains or losses relative to the traditional ensemble approach.

among alternative labels becomes intrinsically more ambiguous, with an expected impact on overall performance.

Moreover, in the 4-class setting, the increased difficulty may also depend on the clinical nature of the labels: the NOS class is intrinsically heterogeneous and, in addition, it may be radiomically less distinct from LCC. This promotes overlap and increases the risk of misclassification between NOS and LCC. In addition, class imbalance (especially the small sample size of NOS) may amplify split-to-split variability and reduce the stability of per-class estimates.

The PCa dataset exhibits a different behavior. Across versions of the dataset with different numbers of selected features, PGM only rarely achieves the top performance. However, even when it is not the best method, its results are often extremely close to those obtained by the ensemble approach, with differences that are frequently very small. This suggests that, in this experimental setting, PGM provides a solid and stable alternative whose performance remains near the strongest baseline, even when it does not take the lead.

Moreover, the per-metric comparison on the PCa dataset highlights an additional point of particular interest: depending on the feature subset, the difference between PGM and the ensemble can take noticeably different values in terms of sensitivity and specificity. In a clinical risk-stratification scenario, this trade-off is relevant: if the primary goal is to minimize false negatives (high-risk cases classified as low-risk), sensitivity should be prioritized; conversely, if the aim is to reduce invasive procedures and overtreatment, higher specificity may be preferable. This, in turn, suggests the possibility of calibrating the method in a cost-sensitive manner (e.g., by acting on priors or on decision rules), thereby aligning the output with clinical priorities.

6 Conclusions

In this work we investigated the application of a quantum-inspired classification strategy based on Pretty Good Measurement (PGM) to radiomic datasets in two clinically relevant scenarios: lung cancer subtyping and prostate cancer risk stratification. The proposed approach was evaluated under the same experimental conditions adopted in previous studies, allowing for a direct and transparent comparison with established machine learning classifiers.

The experimental analysis does not aim to claim a general superiority of PGM over other methods. Rather, our results show that, in specific settings—most notably in the binary and three-class configurations of the NSCLC dataset—the PGM classifier can achieve clearly competitive, and in some cases improved, performance in terms of both accuracy and ROC-based metrics. In more complex configurations, such as the four-class case or in the PCa dataset, PGM does not consistently outperform the strongest baselines; however, its performance remains very close to that of leading ensemble approaches. This consistent competitiveness suggests that PGM should be considered a viable and robust alternative within the set of high-performing classifiers for radiomic tasks.

More broadly, the present study further supports the practical relevance of quantum-inspired methodologies in biomedical imaging. While previous work had already demonstrated the applicability of this framework in binary classification settings, the results reported here extend its use to multi-class problems, showing that the operator-based encoding and measurement strategy can be effectively generalized beyond the simplest scenarios. In this sense, the paper provides additional evidence that quantum-inspired approaches can offer meaningful and practically useful tools for high-dimensional bioimaging applications.

Possible future developments follow naturally from what we have observed. A first step is to clarify more systematically in which regimes the PGM approach tends to yield a performance advantage. Our results suggest that this advantage is not universal, but depends sensitively on the geometry of the problem in the representation space induced by the encoding: in other words, on how the samples from each class are arranged after the operator-valued mapping, and on how much the corresponding class distributions are separated or overlapping. From this perspective, it is natural to complement standard classification metrics with a more direct characterization of the induced geometric structure, for instance via distance/similarity measures between class representatives, overlap indices, and proxies for multi-class separability, and to study how these indicators change when varying the encoding, normalization/scaling parameters, and pre-processing choices. Extending the analysis to additional datasets and multi-class settings would thus help delineate more precisely the conditions under which the PGM rule acts as a favorable inductive bias, and would support a more controlled interpretation of the performance trends as the complexity of the task increases.

At the same time, with a view toward using the method as a support tool, it is useful to complement aggregate performance with an analysis of the error structure, i.e., which class confusions are more likely and how relevant they are from an application-driven standpoint. In biomedical domains, different types of errors may have different downstream consequences; accordingly, a natural extension is to introduce a form of cost-sensitive optimization, in which some confusions are penalized more than others. Operationally, this amounts to moving from an evaluation where all errors are treated as equivalent to one in which the procedure is calibrated to reduce the most critical confusions first, thereby making the classifier’s output more consistent with contextual constraints while preserving the overall methodological framework.

In conclusion, these research directions aim to strengthen both the understanding of the mechanisms that make PGM competitive in the multi-class setting and the robustness and application alignment of the resulting pipeline. Overall, they can help consolidate PGM as a reliable and flexible quantum-inspired component within machine-learning pipelines for biomedical data, while more precisely identifying the use cases in which it represents a particularly effective option.

Acknowledgment

Giuseppe Sergioli and Roberto Giuntini acknowledge financial support from the PRIN-PNRR project “*Quantum Models for Logic, Computation and Natural Processes – Qm4Np*” (code: P2022A52CR), from the PRIN-2022 project “*The COst of Reasoning: Theory and EXperiments – CORTEX*” (code: 2022ZLLR3T) and from the Fondazione di Sardegna project “*An algebraic approach to hyperintensionality*” (code: F23C25000360007).

Roberto Giuntini is partially funded by the TÜV SÜD Foundation, the Federal Ministry of Education and Research (BMBF) and the Free State of Bavaria under the Excellence Strategy of the Federal Government and the Länder, as well as by the Technical University of Munich-Institute for Advanced Study.

Alessandro Stefano and Giorgio Russo acknowledge financial support from the project “The Breast Integrated Solution (BIS): technological innovation to support integrated diagnosis and personalized treatment of breast cancer”, funded by PR FESR 2021/2027, B.U. No. 30 of 27/07/2023 – D.D. No. 320 of 25/07/2023.

References

- [1] Diederik Aerts, Massimiliano Sassoli de Bianchi, and Sandro Sozzo. “On the Foundations of the Brussels Operational-Realistic Approach to Cognition”. In: *Frontiers in Physics* 4 (May 2016). ISSN: 2296-424X. DOI: 10.3389/fphy.2016.00017.
- [2] Diederik Aerts. “Quantum structure in cognition”. In: *Journal of Mathematical Psychology* 53.5 (2009). Special Issue: Quantum Cognition, pp. 314–348. ISSN: 0022-2496. DOI: 10.1016/j.jmp.2009.04.005.
- [3] M.L. Dalla Chiara et al. “The Algebraic Structure of an Approximately Universal System of Quantum Computational Gates”. In: *Foundations of Physics* 39.6 (2009), pp. 559–572. ISSN: 1572-9516. DOI: 10.1007/s10701-009-9302-0.
- [4] Diederik Aerts et al. “Quantum Cognition Beyond Hilbert Space: Fundamentals and Applications”. In: *Quantum Interaction*. Springer International Publishing, 2017, pp. 81–98. ISBN: 9783319522890. DOI: 10.1007/978-3-319-52289-0_7.
- [5] Diederik Aerts et al. “Modeling Human Decision-Making: An Overview of the Brussels Quantum Approach”. In: *Foundations of Science* 26.1 (Mar. 2021), pp. 27–54. ISSN: 1572-8471. DOI: 10.1007/s10699-018-9559-x.
- [6] Diederik Aerts, Massimiliano Sassoli de Bianchi, and Sandro Sozzo. “From quantum cognition to conceptuality interpretation I: tracing the Brussels group’s intellectual journey”. In: *Philosophical Transactions of the Royal Society A: Mathematical, Physical and Engineering Sciences* 383.2309 (Nov. 2025). ISSN: 1471-2962. DOI: 10.1098/rsta.2024.0382.
- [7] Diederik Aerts et al. “Testing Quantum Models of Conjunction Fallacy on the World Wide Web”. In: *International Journal of Theoretical Physics* 56.12 (Dec. 2017), pp. 3744–3756. ISSN: 1572-9575. DOI: 10.1007/s10773-017-3288-8.
- [8] M.L. Dalla Chiara et al. “A many-valued approach to quantum computational logics”. In: *Fuzzy Sets and Systems* 335 (2018). Special Issue: Selected Papers from the 36th Linz Seminar on Fuzzy Set Theory, pp. 94–111. ISSN: 0165-0114. DOI: 10.1016/j.fss.2016.12.015.
- [9] Giuseppe Sergioli et al. “A Quantum-inspired Version of the Classification Problem”. In: *International Journal of Theoretical Physics* 56.12 (Dec. 2017), pp. 3880–3888. ISSN: 1572-9575. DOI: 10.1007/s10773-017-3371-1.
- [10] Giuseppe Sergioli, Roberto Giuntini, and Hector Freytes. “A new quantum approach to binary classification”. In: *PLOS ONE* 14.5 (May 2019), pp. 1–14. DOI: 10.1371/journal.pone.0216224.
- [11] Giuseppe Sergioli et al. “A quantum-inspired classifier for clonogenic assay evaluations”. In: *Scientific Reports* 11.1 (2021), p. 2830. ISSN: 2045-2322. DOI: 10.1038/s41598-021-82085-8.
- [12] Roberto Giuntini et al. “Quantum-inspired algorithm for direct multi-class classification”. In: *Applied Soft Computing* 134 (2023), p. 109956. DOI: 10.1016/j.asoc.2022.109956.
- [13] Roberto Giuntini et al. “Multi-class classification based on quantum state discrimination”. In: *Fuzzy Sets and Systems* 467 (2023), p. 108509. ISSN: 0165-0114. DOI: 10.1016/j.fss.2023.03.012.
- [14] Giovanni Pasini et al. “Phenotyping the Histopathological Subtypes of Non-Small-Cell Lung Carcinoma: How Beneficial Is Radiomics?” In: *Diagnostics* 13.6 (2023). ISSN: 2075-4418. DOI: 10.3390/diagnostics13061167.
- [15] Giovanni Pasini et al. “A Robust [18F]-PSMA-1007 Radiomics Ensemble Model for Prostate Cancer Risk Stratification”. In: *Journal of Imaging Informatics in Medicine* 38.3 (2025), pp. 1388–1402. ISSN: 2948-2933. DOI: 10.1007/s10278-024-01281-w.
- [16] Philippe Lambin et al. “Radiomics: Extracting more information from medical images using advanced feature analysis”. In: *European Journal of Cancer* 48.4 (2012), pp. 441–446. ISSN: 0959-8049. DOI: 10.1016/j.ejca.2011.11.036.
- [17] Alessandro Stefano. “Challenges and limitations in applying radiomics to PET imaging: Possible opportunities and avenues for research”. In: *Computers in Biology and Medicine* 179 (2024), p. 108827. ISSN: 0010-4825. DOI: 10.1016/j.combiomed.2024.108827.
- [18] Geert Litjens et al. “A survey on deep learning in medical image analysis”. In: *Medical Image Analysis* 42 (2017), pp. 60–88. ISSN: 1361-8415. DOI: 10.1016/j.media.2017.07.005.
- [19] Vojtěch Havlíček et al. “Supervised learning with quantum-enhanced feature spaces”. In: *Nature* 567.7747 (Mar. 2019), pp. 209–212. ISSN: 1476-4687. DOI: 10.1038/s41586-019-0980-2.

- [20] Richard Y Li et al. “Quantum processor-inspired machine learning in the biomedical sciences”. In: *Patterns (New York, N.Y.)* 2.6 (June 2021), p. 100246. ISSN: 2666-3899. DOI: 10.1016/j.patter.2021.100246.
- [21] Katarzyna Nałęcz-Charkiewicz, Kamil Charkiewicz, and Robert M Nowak. “Quantum computing in bioinformatics: a systematic review mapping”. In: *Briefings in Bioinformatics* 25.5 (Aug. 2024), bbae391. ISSN: 1477-4054. DOI: 10.1093/bib/bbae391.
- [22] Riddhi S. Gupta et al. “A systematic review of quantum machine learning for digital health”. In: *npj Digital Medicine* 8.1 (May 2025), p. 237. ISSN: 2398-6352. DOI: 10.1038/s41746-025-01597-z.
- [23] Narjust Duma, Rafael Santana-Davila, and Julian R Molina. “Non-Small Cell Lung Cancer: Epidemiology, Screening, Diagnosis, and Treatment”. In: *Mayo Clinic Proceedings* 94.8 (Aug. 2019), pp. 1623–1640. ISSN: 0025-6196. DOI: 10.1016/j.mayocp.2019.01.013.
- [24] Alex Zwanenburg et al. “The Image Biomarker Standardization Initiative: Standardized Quantitative Radiomics for High-Throughput Image-based Phenotyping”. In: *Radiology* 295.2 (2020). PMID: 32154773, pp. 328–338. DOI: 10.1148/radiol.2020191145.
- [25] Fanny Orhac et al. “A Guide to ComBat Harmonization of Imaging Biomarkers in Multicenter Studies”. In: *Journal of Nuclear Medicine* 63.2 (Feb. 2022), pp. 172–179. ISSN: 0161-5505. DOI: 10.2967/jnumed.121.262464.
- [26] Robert Tibshirani. “Regression Shrinkage and Selection via the Lasso”. In: *Journal of the Royal Statistical Society. Series B (Methodological)* 58.1 (1996), pp. 267–288. ISSN: 00359246.
- [27] Dragan Ilic et al. “Prostate cancer screening with prostate-specific antigen (PSA) test: a systematic review and meta-analysis”. In: *BMJ* 362 (2018). ISSN: 0959-8138. DOI: 10.1136/bmj.k3519.
- [28] Hashim U Ahmed et al. “Diagnostic accuracy of multi-parametric MRI and TRUS biopsy in prostate cancer (PROMIS): a paired validating confirmatory study”. In: *The Lancet* 389.10071 (2017), pp. 815–822. ISSN: 0140-6736. DOI: 10.1016/S0140-6736(16)32401-1.
- [29] Giesel F.L. et al. “F-18 labelled PSMA-1007: biodistribution, radiation dosimetry and histopathological validation of tumor lesions in prostate cancer patients”. In: *European Journal of Nuclear Medicine and Molecular Imaging* 44 (2017), pp. 678–688. DOI: 10.1007/s00259-016-3573-4.
- [30] Alessandro Stefano et al. “A fully automatic method for biological target volume segmentation of brain metastases”. In: *International Journal of Imaging Systems and Technology* 26.1 (2016), pp. 29–37. DOI: 10.1002/ima.22154.
- [31] Giovanni Pasini et al. “matRadiomics: A Novel and Complete Radiomics Framework, from Image Visualization to Predictive Model”. In: *Journal of Imaging* 8.8 (2022). ISSN: 2313-433X. DOI: 10.3390/jimaging8080221.
- [32] Joost J.M. van Griethuysen et al. “Computational Radiomics System to Decode the Radiographic Phenotype”. In: *Cancer Research* 77.21 (Oct. 2017), e104–e107. ISSN: 0008-5472. DOI: 10.1158/0008-5472.CAN-17-0339.